



Numerical Study of Water/ Al_2O_3 Nanofluid Forced Convection in a Rotating Hydrophilic and Hydrophobic Microchannel

A. Sohankar^{1†}, M. Riahi¹ and E. Shirani²

¹*Department of Mechanical Engineering, Isfahan University of Technology, Isfahan, 84156-83111, Iran*

²*Foolad Institute of Technology, Fooladshahr, Isfahan 84916-63763, Iran*

†*Corresponding Author Email: asohankar@cc.iut.ac.ir*

(Received April 27, 2018; accepted July 28, 2018)

1. ABSTRACT

In this work, water and water/ Al_2O_3 nanofluid forced convection are studied numerically through a rotating U-shaped microchannel. The hydrophilic (no-slip flow) and hydrophobic (with slip length of $5 \mu\text{m}$) conditions are used on the microchannel walls. Simulations are provided for various nanoparticle volume concentrations ($\phi = 0 - 5\%$), and rotational speeds ($\omega = 0-300 \text{ rad/s}$) and Reynolds numbers ($Re=200-1000$) to study their effects on the pressure drop, heat transfer, and thermal performance coefficient. A modified thermal performance criterion is suggested to include the variations of the working fluid properties relative to the reference case. It is observed that the existence of the nanoparticles in the base fluid provides considerable improvement on the heat transfer. The nanofluid flow also improves the thermal performance coefficient for volume concentrations of $\phi = 0.5\%$ and 2% , while it reduces for $\phi = 5\%$. Although the thermal performance coefficient of the nanofluid flow at $\phi = 5\%$ decreases due to high pressure drop, but it is recommended to use water/ Al_2O_3 at $\phi = 5\%$ as working fluid due to its high heat transfer enhancement (about 40%).

Keywords: U-shaped rotating microchannel; Water/ Al_2O_3 Nanofluid; Volume concentration; Hydrophobic, slip length; Thermal performance.

NOMENCLATURE

A_c	cross-section area	np	nano particle
u_i	velocity components	n	normal vector
C_p	specific heat	s	slip
U_{in}	inlet velocity	NU	local Nusselt number
D	microchannel sides	w	wall
X	x-coordinate	NU_t	average Nusselt number
D_h	hydraulic diameter	PP	power
y	y-coordinate	Δp	pressure drop
E	thermal performance coefficient	δ	smallest grid size
z	z-coordinate	P_e	outlet pressure
G	mass flux	Δ	largest grid size
h	heat transfer coefficient	Pr	Prandtl number
bf	base fluid	ρ	density of the fluid
J	Colburn number	R	bend mean radius
f	equivalent molecular diameter of nanofluid	ν	kinematic viscosity
k	thermal conductivity	r	position vector
i	index, i-component	ϕ	volume concentration of nanofluid particles
Kn	Knudsen number	R_i	bend inner radius
nf	nanofluid	Re	Reynolds number
L_t	temperature jump length	S	length in flow direction
ref	reference value or case	T	temperature
M	Molecular weight	T_b	bulk temperature of fluid
pw	pure water		
N	Avogadro constant		

1. INTRODUCTION

Serious attempts have been made to apply various active and passive methods to increase heat transfer in thermal systems. These various augmentation techniques can provide substantial energy savings, more compact and less expensive apparatus with higher thermal efficiency (Bergles 1997, 2000; Webb and Kim 2005; Saha *et al.* 2012; Mirzaei *et al.* 2013a, 2014; Behfard 2016). Using array of microchannels instead of macrochannel, hydrophobic surfaces (surfaces that expels water) as well as nanofluids as working fluid can consider as suitable and promising methods for achieving these goals (Kanikzadeh and Sohankar 2016a, 2016b; Sohankar *et al.* 2017). The type of working fluid employed in a thermal system has severe restrictions in many applications. The conventional heat transfer fluids, such as air, water and engine oil, have limited capabilities in terms of thermal properties. Most solids, in particular metals, have thermal conductivities much higher compared to those of liquids. Thus, it is expected that fluid containing solid particles to significantly increase the effective conductivity and heat transfer. Size decreasing of a thermal system has the remarkable advantages in comparison with the conventional size. For example, the rotating macrochannels were used in many applications such as cooling of the gas turbine blades (Al-Qahtani *et al.* 2002). Using array of rotating microchannels instead of a macrochannel can improve the thermal performance significantly (Kanikzadeh and Sohankar 2016a,b; Sohankar *et al.* 2017). It should be noted that the slip flow could be occurred in microscale devices with gases and liquids as working fluids. The various flow regimes for gas flow can be identified by a non-dimensional parameter, i.e. the Knudsen number (Kn) which is the ratio of mean free path of fluid molecules and characteristic length (Karniadakis *et al.* 2005).

Slip gas flow in non-circular microchannels was investigated by Duan and Muzychka (2007). They proposed a simple model for predicting the friction factor in various non-circular microchannels for slip flow, $Kn < 0.1$. Xiao *et al.* (2009) applied second order slip and temperature jump boundary conditions to simulate the gas flow and heat transfer in a microtube. It was found that the second-order boundary conditions, assuming an effective mean free path model predict a lower slip velocity than a first-order model assuming hard sphere mean free path model.

Most studies for flow through microchannels with velocity slip and temperature jump boundary conditions were reported at low Reynolds numbers. On the other hand, the liquid slip can occur even when the continuum regime is valid due to using a coated or structured solid wall (Watanabe and Mizunuma 1998; Choi *et al.* 2002; Trethway and Meinhart 2002; Arkles 2011). In this condition, the Navier Stokes equations are usually employed for liquid flow with the hydrophilic surface (no-slip condition) or hydrophobic or superhydrophobic surface (slip condition) (Kalteh *et al.* 2012; Kundu *et al.* 2009; Raisi *et al.* 2011; Roy *et al.* 2013a,b; Cowley *et al.* 2014, Sohankar *et al.* 2017).

Lee and Mudawar (2007) experimentally evaluated effectiveness of Al_2O_3 nanofluid for single-phase and two-phase heat transfer in microchannels. They concluded that Al_2O_3 nanoparticles have an effect less than 5% (mainly less than 2%) for enhancing single-phase and two-phase flow and heat transfer in microchannel heat sinks for $Re \leq 1000$. They showed that the nanoparticle concentration increases the single-phase pressure drop and heat transfer compared to pure fluids at the same Reynolds number. Kundu *et al.* (2009) simulated the liquid flow in the microchannel with slip boundary condition ($1 < Re < 25$). Choi *et al.* (2002) developed experimentally a slip length model for liquid flow in microchannel. They reported that the friction force reduces due to the slip effect. Numerical study of the thermal performance of a microchannel (2.5mm length and $2h=50\mu m$ hydraulic diameter), cooled with either pure water or a Cu-water nanofluid, with considering the effects of both no-slip and first order slip boundary conditions on the flow field and heat transfer conducted by Raisi *et al.* (2011). They studied the effects of pertinent parameters such as Reynolds number (from 10 to 500), solid volume fraction, and slip velocity coefficient on the thermal performance of the microchannel. They indicated that for low values of Reynolds number ($Re=10$), the volume concentration shows negligible influence on the heat transfer rate; however, at high values of Reynolds number ($Re=500$), the heat transfer rate increases with increasing the volume concentration. In addition, the slip boundary condition shows no effect on the heat transfer rate at low Reynolds numbers while, at high Reynolds numbers, the heat transfer rate increases as the slip velocity coefficient is increased. Finally, they concluded that the slip boundary condition is important factor in the analysis of nanofluid thermal performance. Therefore, the correct value of slip velocity coefficient should be accurately considered in the analysis in order to achieve reliable results. Water and water/ Al_2O_3 nanofluid (homogeneous and two-phase) forced convection inside a wide microchannel heat sink (94.3 mm, 28.1 mm and 580 mm; length, width and height, respectively) was investigated experimentally and numerically for $Re \leq 300$ by Kalteh *et al.* (2009). The no-slip hypothesis was assumed in the mentioned study. The maximum deviations from experimental results were observed to be about 12.61 and 7.42 % for homogeneous and two-phase results, respectively. Roy *et al.* (2013a) have studied the slip flow and heat transfer in a rotating straight rectangular microchannel numerically. A reduction of about 28.5-30 percent in hydrodynamic resistance was observed using $10\mu m$ slip length for various channels aspect ratios from 1 to 20 and for $Re=100$. Roy *et al.* (2013b) also published a review on the recent advances in the area of flow and heat transfer applications in rotating microchannels. Cowley *et al.* (2014) investigated thermal transport in a parallel-plate channel with superhydrophobic walls numerically. In this study, some results have been obtained for a range a Peclet numbers between 1-10,000 and Prandtl number corresponding to water for slip

length calculations and compared with analytical work performed by *Maynes et al.* (2013). They reported that the overall heat transfer rate for a superhydrophobic channel was less than that of classical channel for all scenarios considered. *Maynes and Crockett* (2014) also provided an analytical investigation of thermal transport in a parallel-plate channel comprised of metal superhydrophobic walls. Nanofluids heat transfer in a ribbed microchannel ($0.215 \times 0.821 \times 44.8 \text{ mm}^3$) heat sink using two single-phase and multiphase CFD models were investigated by *Yari Ghale et al.* (2015). They used water/ Al_2O_3 nanofluid as working fluid for less than 2% volume concentrations. They concluded that the two-phase model is more precise than the single-phase model. Difference between the experimental results (*Lee and Mudawar* 2007) and their numerical study for single and two-phase simulations for heat transfer characteristics is more pronounced. According to the CFD predictions, it was found that in the ribbed microchannel, both friction coefficients and Nusselt numbers are higher than those in a channel without ribs. *Sohankar et al.* (2017) reported the results of heat transfer and pressure drop in a rotating U-shaped microchannel, $\text{Re}=200\text{-}1000$. Effects of parameters including the rotational speed, slip flow, temperature jump were investigated on the heat transfer, pressure drop and thermal performance coefficient. They reported an improvement on the heat transfer and a large reduction on the pressure drop, when the slip length increases from zero to $10 \text{ }\mu\text{m}$. In addition, an increase about 90% was found for the thermal performance coefficient for $10\text{-}\mu\text{m}$ slip length in comparison with that of no-slip condition.

In the present work, the effects of water/ Al_2O_3 nanofluid, the hydrophilic and hydrophobic wall surfaces, rotational speed and Reynolds number are investigated in a U-shaped microchannel. Simulations were provided for various nanoparticle volume concentrations ($\phi=0\text{-}5\%$), rotational speeds ($0\text{-}300 \text{ rad/s}$) and Reynolds numbers ($\text{Re}=200\text{-}1000$) to study their effects on the heat transfer, pressure drop and thermal performance coefficient. In fact, the selected limits of these parameters in this study are approximately in the range of those employed in similar works for microchannels. To judge about the suitability of the results, a modified thermal performance criterion is used as a reasonable balance between the heat transfer enhancement and the pressure drop or power consumed to include the variations of the working fluid properties relative to the reference case.

2. GEOMETRICAL CONFIGURATION, GOVERNING EQUATIONS AND NUMERICAL DETAILS

Figure 1(a) depicts the geometrical configuration under consideration. It consists of the flow and heat transfer of water/ Al_2O_3 nanofluid flowing inside a three-dimensional rotating U-shaped microchannel with square cross-section ($D \times D$), where

$D=D_h=150\mu\text{m}$. The flow with uniform temperature and velocity profiles enters into the microchannel in the opposite of x-direction at $x=0$, while it exits in x-direction. The microchannel rotates in y-direction in the range of $\omega=0\text{-}300 \text{ rad/s}$. The straight length and inner radius of the channel curve are selected as $53.3D$ and $13.5D$, respectively. The microchannel length is denoted with S , where $S/D=0$ and $S/D=151.7$ are located at the inlet and outlet, respectively. Three sections are selected along the microchannel to show some results in these cross-sections, i.e. midsection of the first pass ($S/D=30$), bend region ($S/D=75.85$) and midsection of the second pass ($S/D=121.7$). The Reynolds number ($\text{Re}=\rho U_{in} D_h / \mu$) based on inlet velocity, U_{in} , and hydraulic diameter, D_h , is in the range of $\text{Re}=200\text{-}1000$. It should be noted that the hydraulic diameter is equal to the side length of the square cross-section, $D_h=D$.

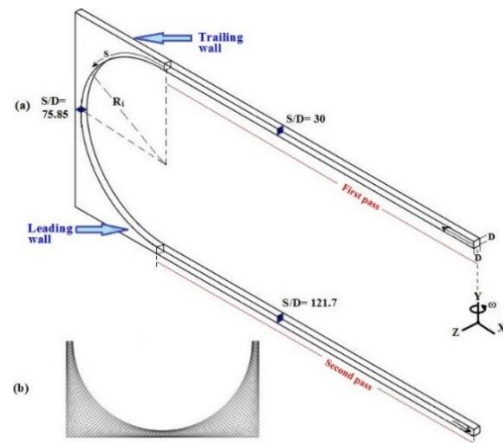


Fig. 1. (a) Geometrical configuration under consideration (a three-dimensional rotating U-shaped microchannel), (b) grid distribution in the bend region.

The governing equations (continuity, momentum and energy equations) for rotational system with steady and laminar flow, constant properties, three-dimensional and incompressible flow assumptions are as Eqs. (1) - (3). The effect of viscous dissipation in energy equation is neglected. The commercial software (Fluent) is employed for simulations.

$$\frac{\partial u_i}{\partial x_i} = 0 \quad (1)$$

$$\frac{\partial(u_i u_j)}{\partial x_j} = -(1/\rho) \frac{\partial p}{\partial x_i} + \nu \frac{\partial^2 u_i}{\partial x_j \partial x_j} - 2\varepsilon_{ijk} \omega_k u_j - (\omega_j \omega_i r_j - \omega_j \omega_j r_i) \quad (2)$$

$$\frac{\partial(u_j T)}{\partial x_j} = \frac{k}{\rho c_p} \frac{\partial^2 T}{\partial x_j \partial x_j} \quad (3)$$

In Eq. (2), r is position vector from the axis of rotation. The third and fourth terms in the right side of Eq. (2) are the centrifugal and Coriolis forces, respectively.

At the inlet of microchannel, uniform fluid velocity

and temperature profiles are considered as boundary conditions. At the exit section, a known ambient pressure is imposed and zero temperature gradient is used. On the microchannel walls, the slip velocity of fluid and temperature jump is imposed (Karniadakis *et al.* 2005; Sohankar *et al.* 2017), see Eqs. (4) and (5).

$$u_s - u_w = L_s \left. \frac{\partial u}{\partial x_i} \right|_w \quad (4)$$

$$T_s - T_w = L_t \left. \frac{\partial T}{\partial x_i} \right|_w \quad (5)$$

In the Eq. 4, u_s is the slip velocity of fluid on the walls, u_w is the wall velocity and L_s is the slip length. In Eq. 5, T_s and T_w indicate the fluid temperature at the wall and the wall temperature, respectively. In this equation, L_t is the temperature jump length, as a thermal resistance length at the solid-liquid interface (Barrat and Chiaruttini 2003). It should be noted that this length has a relationship with slip length via Prandtl number (Pr) as $L_t = L_s/Pr$ (Barrat and Chiaruttini 2003; Karniadakis *et al.* 2005; Roy *et al.* (2013a)). In fact, the Prandtl number of water or nanofluid is high, thus L_t is smaller than L_s . Therefore, it is expected that the temperature jump length becomes less important in comparison with that of the slip length.

As noted earlier, to judge about the suitability of a thermal system, a balance between the power consumed and heat transfer augmentation via a thermal performance coefficient was used by many researchers (Shah and Sekulic 2003; Sohankar 2007, Mirzaei and Sohankar 2013a; Mirzaei *et al.* 2014). The formulas used for thermal performance coefficients were extracted based on similar properties for two flows considered (main flow and reference flow). In some cases, this assumption is correct, e.g. using the same fluid for a channel with ribs (main flow) and without them (reference flow). When two different fluid flows are compared in a thermal system (e.g. water and water/ Al_2O_3 nanofluid), such relations need some modification to include the physical properties of two fluids.

Equations (6) and (7) introduce the heat transfer coefficient (h) and the pumping power (PP); and they are employed to obtain the modified relation for thermal performance coefficient. Based on Eq. (6), the ratio of hA for two cases, are presented in Eq. (8), where A is the heat transfer area.

$$h = C_p Pr^{-2/3} JG \quad (6)$$

$$PP = \frac{\dot{m}\Delta p}{\rho} = \Delta p A_c U = \left(\frac{fAG^2}{2A_c\rho} \right) \left(\frac{GA_c}{\rho} \right) \quad (7)$$

$$\frac{(hA)}{(hA)_{ref}} = \left(\frac{J}{J_{ref}} \right) \left(\frac{A}{A_{ref}} \right) \left(\frac{G}{G_{ref}} \right) \left(\frac{C_p}{C_{p,ref}} \right) \left(\frac{Pr}{Pr_{ref}} \right)^{-2/3} \quad (8)$$

In Eqs. (6) to (8), J is the Colburn factor and G is the mass velocity (ρU). In addition, A_c and U are the

flow cross-sectional area and velocity, respectively. In Eq. (8), the reference parameters depend on the case used for comparison, e.g. the pure water, no-slip condition, etc.

If the temperature differences for calculating heat transfer are considered similar for two cases, then the left side of the Eq. (8) is the heat transfer ratio. The ratio of power consumption (Eq. (7)) to that of reference case is obtained as Eq. (9).

$$\frac{PP}{PP_{ref}} = \left(\frac{f}{f_{ref}} \right) \left(\frac{A}{A_{ref}} \right) \left(\frac{\rho}{\rho_{ref}} \right)^{-2} \left(\frac{G}{G_{ref}} \right)^3 \quad (9)$$

By eliminating the mass velocity, G , between the Eqs. (8) and (9), general form of the thermal performance coefficient is obtained as Eq. (10). This formula is a general relation for finding thermal coefficient as a balance between the heat transfer enhancement and the pressure drop or power consumed. Equation (11) expresses the variations of the working fluid properties relative to the reference case. If the performance coefficient is obtained for a specific working fluid for two cases, thus $C=1$ and Eq. (12) is used for such conditions (Shah and Sekulic 2003; Kanikzadeh and Sohankar 2016a,b; Sohankar *et al.* 2017).

$$E = \frac{\frac{(hA)}{(hA)_{ref}}}{\left(\frac{PP}{PP_{ref}} \right)^{1/3} \left(\frac{A}{A_{ref}} \right)^{2/3}} = \frac{\frac{(J)}{(J)_{ref}}}{\left(\frac{f}{f_{ref}} \right)^{1/3}} \times C \quad (10)$$

$$C = \left(\frac{\rho}{\rho_{ref}} \right)^{-2/3} \left(\frac{C_p}{C_{p,ref}} \right) \left(\frac{Pr}{Pr_{ref}} \right) \quad (11)$$

$$\frac{\frac{(hA)}{(hA)_{ref}}}{\left(\frac{PP}{PP_{ref}} \right)^{1/3} \left(\frac{A}{A_{ref}} \right)^{2/3}} = \frac{\frac{(J)}{(J)_{ref}}}{\left(\frac{f}{f_{ref}} \right)^{1/3}} \quad (12)$$

For cases with two different fluids (e.g. water and water/ Al_2O_3 nanofluid), or when the performance of different working fluids are compared, C -coefficient becomes a value other than unity and Eq. (10) should be employed for finding the thermal performance coefficient. The left side of Eq. (10) is introduced as the thermal performance coefficient (E). Equation (10) illustrates that the heat transfer improvement provides under constant power and heat transfer area, when the thermal performance coefficient is greater than one. A simplified version of Eq. (12) was introduced for obtaining the thermal performance coefficient for a thermal system with fluid and nanofluid (Suresh *et al.* 2011; Manca *et al.* 2012; Yari Ghale *et al.* 2015), where $J = StPr^{2/3}$, $St = Nu/(RePr)$, see Eq. (13).

$$E = \frac{\frac{(NU)}{(NU)_{ref}}}{\left(\frac{f}{f_{ref}} \right)^{1/3}} \quad (13)$$

The Eq. (13) is obtained by simplifying the right side of Eq. (12) with assuming the same Reynolds and

Prandtl numbers for the reference and main fluid flows. If the main and reference fluids are not similar, using Eqs. (13) or (12) can provide rough estimation of the thermal performance coefficient. For such cases, Eq. (10) should be employed.

The local Nusselt number is defined as Eq. (14), where T_b and T_w are the local bulk temperature and the wall temperature, respectively.

$$Nu = \frac{D_h \left(\frac{\partial T}{\partial n} \right)_w}{T_w - T_b} \quad (14)$$

It is important to determine the accurate equivalent physical properties in a single-phase nanofluid. The most convenient model can predict the parameters affecting the properties of a nanofluid (such as density, thermal conductivity and viscosity). Weight functions are generally defined for the density and volumetric heat capacity (Eqs. (15) and (16)) and are only related to the volume fraction of particles (Kalteh *et al.* 2009; Vajjha and Das 2009; Kanikzadeh and Sohankar 2016a), where ϕ is the concentration of nanoparticles.

$$\rho_{nf} = (1-\phi) \rho_{bf} + \phi \rho_{np} \quad (15)$$

$$(\rho c_p)_{nf} = (1-\phi)(\rho c_p)_{bf} + (\rho c_p)_{np} \phi \quad (16)$$

Vajjha and Das (2009) proposed experimental relations (Eqs. 17,18) for determining the thermal conductivity coefficient for nanofluids by taking into account the parameters such as particle sizes, volume fraction of particles, temperature and properties of base fluid and nanoparticles as well as effects of Brownian motion (Vajjha and Das 2009) :

$$k_{nf} = \frac{k_{np} + 2k_{bf} - 2(k_{bf} - k_{np})\phi}{k_{np} + 2k_{bf} - (k_{bf} - k_{np})\phi} k_{bf} + \quad (17)$$

$$5 \times 10^4 \beta \phi \rho_{bf} C_{p, bf} \sqrt{\frac{kT}{\rho_{np} d_{np}}} f(T, \phi)$$

$$f(T, \phi) = \left(2.8217 \times 10^{-3} \phi + 3.917 \times 10^{-3} \right) \left(\frac{T}{T_0} \right) + \quad (18)$$

$$\left(-3.0669 \times 10^{-2} \phi - 3.91123 \times 10^{-3} \right)$$

Where $T_0=273K$, and β is a coefficient different for each nanofluid. They proposed β for nanoparticles of CuO and Al_2O_3 (Vajjha and Das 2009).

Corcione *et al.* (2013) proposed nanofluids viscosity relation as Eq. (19), where d_{np} is the nanoparticles diameter, M is molecular weight, N is the Avogadro constant and d_f is equivalent molecular diameter of nanofluid which is determined using the Eq. (20):

$$\frac{\mu_{nf}}{\mu_{bf}} = \frac{1}{1 - 34.87 \left(\frac{d_{np}}{d_f} \right)^{-0.3} \phi^{1.03}} \quad (19)$$

$$d_f = \left(\frac{6M}{N \pi \rho_{bf} 0} \right) \quad (20)$$

where ρ_{bf0} is the base fluid density at $T_0=273 K$. Equation (19) can be used to determine the viscosity of the two nanofluids water/ Al_2O_3 and water/ TiO_2 (Corcione *et al.* 2013).

In this work, the water/ Al_2O_3 is selected as a working fluid and the Eqs. (15)-(19) are used to determine its properties. In fact, the behavior of a nanofluid depends on the type and dimensions of problem under consideration, range of Reynolds number and temperature changes, Brownian motion and the size of nanoparticles. These factors should be considered for finding a suitable model. Vajjha and Das (2009) model for calculating the thermal conductivity of water/ Al_2O_3 nanofluid has been used by considering the effects of Brownian motion. This point is important for rotational channels or special geometries, i.e. curved and ribbed channels (Vajjha and Das 2009; Corcione *et al.* 2013; Kanikzadeh and Sohankar 2016a). Previous works reported that the water/ Al_2O_3 nanofluid has a good thermal performance in many flow problems (Vajjha and Das 2009; Kalteh *et al.* 2009; Hung *et al.* 2012; Corcione *et al.* 2013; Kanikzadeh and Sohankar 2016a,b).

3. GRID STUDY

The grid independence test is carried out to ensure the accuracy and reliability of the numerical simulations. Figure 1(b) shows the grid distribution in the bend region of the microchannel. In this study, four different grids are selected for water as working fluid, i.e. G1 ($12 \times 12 \times 348$), G2 ($14 \times 14 \times 515$), G3 ($16 \times 16 \times 976$) and G4 ($20 \times 20 \times 1200$). Then, the best grids are also examined for nanofluid as working fluid. The smallest (δ/D) and largest (Δ/D) grid size employed are provided in Table 1. The lengths are scaled with the hydraulic diameter ($D=150 \mu m$), and the smallest grid size is placed near the walls. The pressure drop and Nusselt number for microchannel for different grids are also compared in Table 1 ($Re=200$, $\omega=200$ rad/s (rotational speed), and $L_s=1 \mu m$ (slip length)). The results for pure water in this table for grids G3 and G4 show very close agreement. The grid independency test is also performed for $Re=1000$ and it is found that grid 3 (G3) also provides suitable results for pure water as a working fluid (see Table 1).

Based on this grid study for water, it is concluded that the grids 3 and 4 provides very close agreement. Thus these grids also tested for nanofluids flow ($Re=1000$) and a good agreement is observed, see Table 1. Figure 2 illustrates the local Nusselt numbers of nanofluid flow, $\phi=5\%$ along the channel length (denoted with S , see Fig. 1(a)) for four grids introduced in Table 1. Again, the differences between the results

Table 1 Grid independency study for $\omega=200$ rad/s, $L_s=1\mu\text{m}$.

Name	Re	Grid (y×z×s)	$\frac{\delta}{D}$	$\frac{\Delta}{D}$	NU _T	% Diff	ΔP_T (kpa)	% Diff
G1 _{pw}	200	12×12×348	0.06	0.09	5.58	---	14.445	---
G2 _{pw}	200	14×14×515	0.05	0.09	5.36	4.1	14.685	1.66
G3 _{pw}	200	16×16×976	0.04	0.08	5.22	2.7	14.928	1.65
G4 _{pw}	200	20×20×1200	0.03	0.07	5.21	0.2	15.054	0.84
G3 _{pw}	1000	16×16×976	0.04	0.08	9.49	---	114.46	---
G4 _{pw}	1000	20×20×1200	0.03	0.07	9.41	0.84	115.90	1.2
G3 _{nf, $\phi=5\%$}	1000	16×16×976	0.04	0.08	12.19	---	279.49	---
G4 _{nf, $\phi=5\%$}	1000	20×20×1200	0.03	0.07	11.93	2.11	273.55	2.12

of G3 and G4 are negligible. Thus, it is concluded that grid 3 (G3) provides suitable results for both the pure water and water/Al₂O₃ nanofluid flow, $\phi = 5\%$, see Table 1 and Fig. 2. According to the negligible differences between the results for grids G3 and G4 (less than 2.2 % for all results) and a saving on the computational time, Grid 3 (G3) is employed for all further simulations.

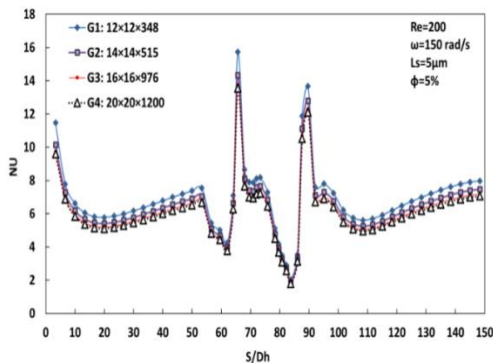


Fig. 2. Local Nusselt number of nanofluid flow, $\phi = 5\%$, along the microchannel length (denoted with S, see Fig. 1) for four grid sizes introduced in Table 1.

4. VALIDATION

In our previous work (Sohankar *et al.* 2017), the similar configuration was adapted with water as working fluid. Due to lack of validation cases and in order to confidence about the accuracy of the obtained results, a configuration was adopted similar to that employed by Tretheway and Meinhart (2002) in their experimental work. A good agreement between their results (no-slip/slip) of Sohankar *et al.*

(2017) and experiment performed by Tretheway and Meinhart (2002) was reported. In addition, a good agreement was observed between the results of Sohankar *et al.* (2017) and a configuration was adopted similar to that numerically performed by Roy *et al.* (2013a). These validation cases were performed only for water as working fluid to study the effect of slip/no-slip conditions. To validate our results for nanofluid as working fluid, the experimental work of Kalteh *et al.* 2012 was adopted as new validation case. In Kalteh *et al.* (2012), the water and water/Al₂O₃ nanofluid flows (nanoparticle diameter about 40 nm) were used inside a stationary microchannel with cross sectional dimensions of 28.1×0.58 mm² and length of 94.3 mm for Reynolds number in range of 50-300. In the present study, a 2D simulation with 600×90 mesh grids was implemented to study the same geometry of Kalteh *et al.* (2012) for the nanofluid with the properties were introduced by Eqs. (15)-(19). Figure 3 compares the Nusselt numbers and a good agreement is obtained for pure water in this study and those of the experimental work (Kalteh *et al.* 2012) with a difference less than 2% for all cases. The differences between the numerical and experimental results (Kalteh *et al.* 2012) for nanofluid with volume fractions of 0.1% and 0.2% at the higher Reynolds numbers were about 12 and 14.5 %, respectively. These differences between numerical and experimental results are not so high for single-phase (homogenous) nanofluid hypothesis flow models. Based on the validation study, it is expected to find relatively suitable results with the single-phase (homogenous) nanofluid model employed for the problem under consideration of this work. For obtaining more accurate results especially for higher concentrations of nanoparticles, it is necessary to use two phase models.

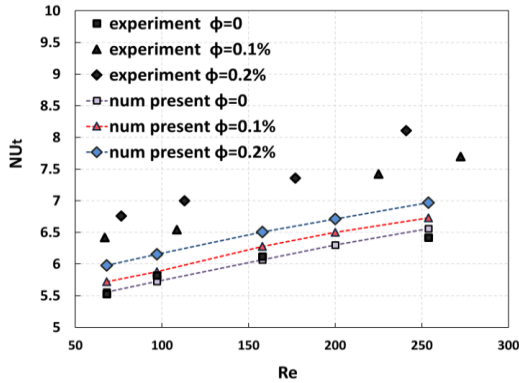


Fig. 3. Comparison of average Nusselt numbers obtained from the present work and the experimental study [25].

It should be emphasized again a homogenous model has been used where the thermophoresis forces are not considered. In fact, more accurate results may obtain by considering the Brownian and thermophoresis forces (Eslamian and Ziad saghir 2014; Ahmed and Eslamian 2015). In addition, the trajectory of the nanoparticles cannot be detected with a homogenous model. In reality, the sedimentation and blocking of the channel can occur especially at the curve regions for higher ϕ , e.g. $\phi = 5\%$. This can cause the nanoparticles may tend to become separated from the fluid (Eslamian *et al.* 2015). In general, a homogenous model is not sufficient for providing the details of trajectory of the nanoparticles, although it can provide relatively accurate results for some parameters such as pressure drop and Nusselt number.

5. RESULTS AND DISCUSSIONS

In the present work, the influence of several parameters are investigated including the type of working fluid (pure water and water/ Al_2O_3 nanofluid), wall hydrophobicity with slip length of $L_s = 5\mu\text{m}$ and temperature jump boundary condition for $\text{Re} = 200\text{-}1000$ and $\omega = 0\text{-}300$ rad/s. The results for velocity/temperature profiles, pressure drop and heat transfer rate are provided and compared for aforementioned parameters and will be presented below.

Figure 4 shows the scaled x-velocity profiles of pure water and water/ Al_2O_3 nanofluid for a slip length along the z-axis ($Y = R_i + D/2$, Fig. 4(a)) and y-axis (Fig. 4(b)) at the two sections ($S/D = 30$, $S/D = 121.7$), see also Fig. 1(a). This figure is provided for both fluids with a same Reynolds number ($\text{Re} = 600$). Because the fluid properties of two fluids are not the same, thus different inlet velocities are used for providing a similar Reynolds number. This difference causes that the velocity for nanofluid at each position along the microchannel becomes higher than that of water. In spite of this difference, the variation trends of velocities for both fluids are similar along the channel. As shown from Fig. 4(a), the peak of velocity profiles in the first pass ($S/D = 30$) for both fluids are deviated to the trailing wall,

while they shift to the leading wall in the second pass ($S/D = 121.7$). The Coriolis force in the first pass and both effects of the Coriolis force and bend are the main reasons of such velocity variations. The slip-velocity values at the microchannel walls ($z/D = -0.5$ and $z/D = 0.5$) are seen in Fig. 4(a), where their maximum and minimum values at $S/D = 30$ occur on the trailing ($z/D = -0.5$) and leading ($z/D = 0.5$) walls, respectively (see also Fig. 1). In addition, the walls slip-velocities have similar values at the inner ($y/D = \pm(13.34)$) and outer walls ($y/D = \pm(14.34)$). Fig. 4 (a) and (b) indicates that the peak of velocity profiles in the midsection of first pass ($S/D = 30$) has larger value than that of second pass due to its higher slip velocity on the walls.

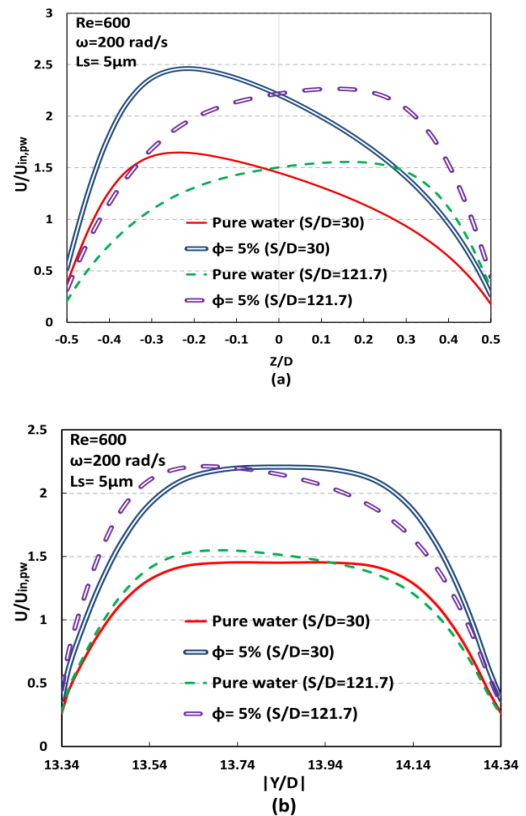


Fig. 4. Velocity profiles of pure water and water/ Al_2O_3 nanofluid (normalized with the pure water inlet velocity) at the midsection of the first pass ($S/D = 30$) and second pass ($S/D = 121.7$), (a) along the z-axis ($Y = R_i \pm D/2$) and (b) y-axis.

Figure 5 shows the slip velocity (normalized with respect to the pure water inlet velocity) profiles on the leading and trailing walls in: (a) first pass ($S/D = 30$), and (b) second pass ($S/D = 121.7$) of the microchannel. This figure is provided for both fluids at a slip length of $5\mu\text{m}$. As seen, the wall slips velocity of the nanofluid flow in both passes increases as compared with that of the pure water flow case. It should be noted that these results are reported for $\text{Re} = 400$ for both fluids which provides a higher inlet velocity for nanofluids by about 70% ($\phi = 5\%$) compared with that of pure water due to the higher viscosity of nanofluid. Thus, a part of the

difference between slip velocities of both fluids (Fig. 5) is due to the difference in their inlet velocities. This causes that the velocity gradients of the nanofluid on the walls increase, then the slip velocity increases for a constant slip length (see Eq. (4)).

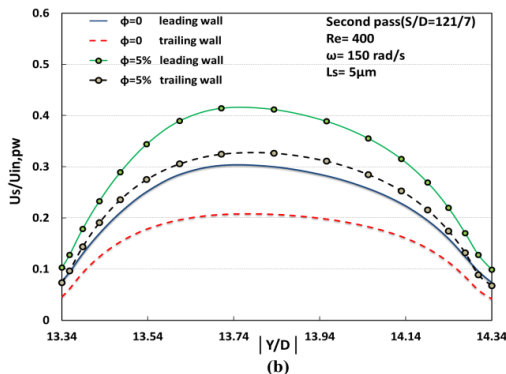
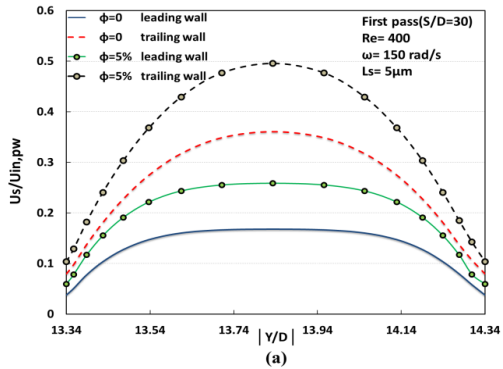


Fig. 5. The slip velocity (normalized with respect to the pure water inlet velocity) profiles on the leading and trailing walls in: (a) first pass ($S/D=30$), and (b) second pass ($S/D=121.7$).

Figure 6 shows the scaled temperature profiles at the centerline of microchannel parallel to the z -axis in three positions along the channel in the first pass, second pass, and symmetry section of the bend region. The temperature contours at the plane of symmetry of the microchannel ($z=0$) for both fluid are shown in Fig. 7. This figure shows that the temperature difference between fluid and wall along the microchannel decreases. It becomes approximately uniform in the second pass, while it is non-uniform in the first pass where the minimum value is deviated to the trailing wall, see Fig. 6. In fact, the percent of heat transfer in the second pass is much less than that of the first pass and the bend region. In addition, the temperature difference between the nonofluid and wall at each position along the microchannel is lower than that of the pure water, see Figs. 6 and 7.

The average Nusselt number, heat transfer rate, pressure drop and thermal performance coefficient of the microchannel are presented below for various nanoparticle volume concentrations, rotational speeds and fluids (pure water and water/ Al_2O_3 nanofluid).

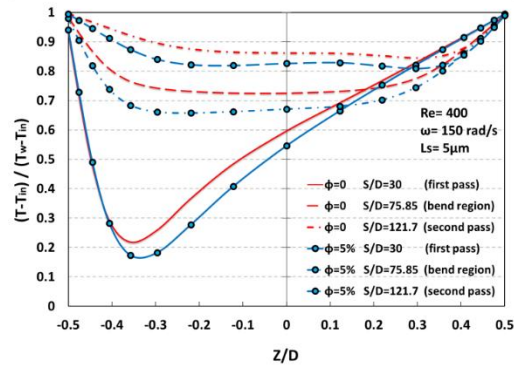


Fig. 6. The scaled temperature profiles for pure water and water/ Al_2O_3 flows ($\phi = 5\%$) at the centerline of microchannel parallel the z -axis in three sections, first pass ($S/D=30$), symmetry section of the bend region and the second pass ($S/D=121.7$).

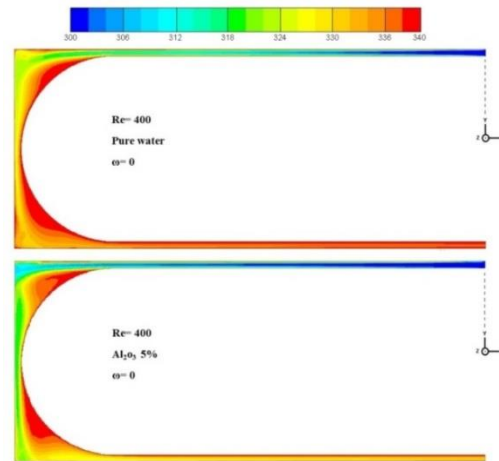


Fig. 7. The temperature contours at the plane of symmetry of the microchannel ($z=0$) for pure water and water/ Al_2O_3 ($\phi = 5\%$).

Figure 8 shows the average Nusselt number variations for different rotational speeds, Reynolds numbers and volume concentrations. The average Nusselt number variation with the rotational speed and volume concentration of nanofluid ($Re=400$, $L_s=5 \mu m$) is illustrated in Fig. 8(a). As seen, the average Nusselt number increases with increasing the rotational speed and volume concentration of nanofluid. This increase is about 27 % from $\phi = 0$ to $\phi = 5\%$ at rotational speed of 300 rad/s. Figure 8(b) shows the average Nusselt number variation with Reynolds number and volume concentration of nanofluid ($\omega=0$ and 300 rad/s, $L_s=5 \mu m$). As seen, the average Nusselt numbers increase with increasing the Reynolds number from 200 to 1000, where this increase reaches to about 110% in the stationary microchannel for both flows. Similarly, this increase is about 80% for both pure water and water/ Al_2O_3 ($\phi=5\%$) flows. Figure 8(c) shows the average Nusselt number variations for slip lengths of $L_s=0$ (no-slip) and $L_s=5 \mu m$, various rotational speeds and volume concentrations (scaled with those of pure water at the corresponding rotational speed), $Re=400$. It is seen that the average Nusselt number of nanofluid ($\phi =$

5%) increases between 23 to 33 % for different rotational speeds as compared with those of pure water flow. Clearly, it is observed that using nanofluid has significant effect on the heat transfer improvement.

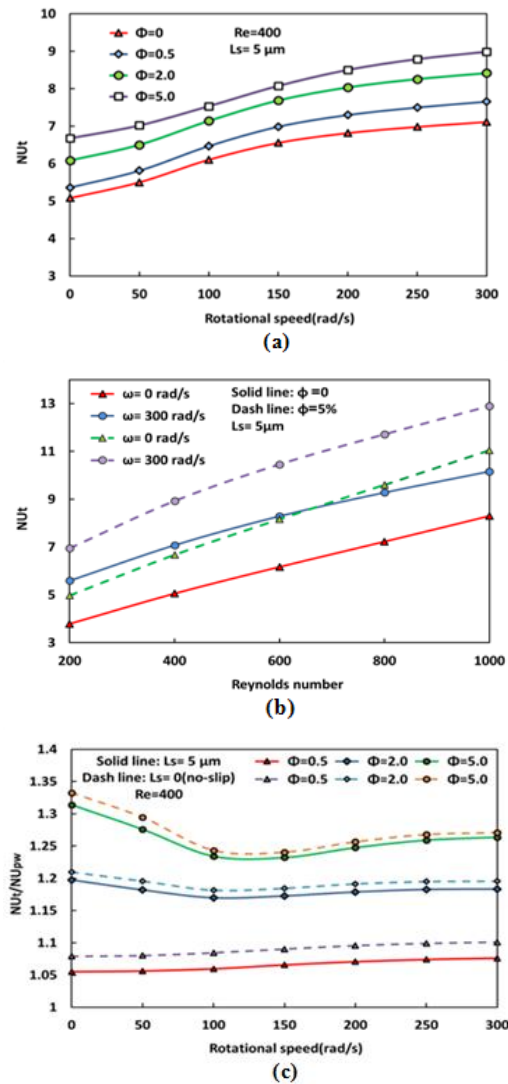


Fig. 8. The average Nusselt number variation with (a) the rotational speed and volume concentration of nanofluid ($Re=400, L_s=5 \mu m$), (b) Reynolds number and volume concentration of nanofluid ($\omega=0$ and $300 \text{ rad/s}, L_s=5 \mu m$), (c) slip lengths of $L_s=0$ (no-slip) and $L_s=5 \mu m$, various rotational speeds and volume concentrations.

Figure 9 (a) shows the share of average heat transfer rate in the first pass, second pass and bend region of the microchannel ($Re=400, \omega=300 \text{ rad/s}, L_s=5 \mu m$). These results are normalized with respect to the average heat transfer of the microchannel for the corresponding fluid. As seen, the most of heat transfer occurs at the first pass and bend-section for both fluids (about 92%), see also Figs. 6 and 7. The heat transfer of the second pass is less than 8% due to the reduction of temperature difference between fluid and wall. The role of nanofluid and water on the heat transfer rate is more important in the bend

region and first pass, respectively.

In Fig. 9(b), the average heat transfer of nanofluid is compared at $Re=200$ and $Re=1000$ for different volume concentrations, ϕ . These results are scaled with the average heat transfer of the pure water flow for the corresponding Reynolds number. As seen, the heat transfer rate increases about 42% at $Re=200, \phi = 5\%$ when it is compared with that of pure water flow. This increase is about 37% at $Re=1000, \phi = 5\%$. However, for the nanofluid with lower concentration ($\phi = 5\%$ and 2%), the increased heat transfer at $Re=1000$ is more than that obtained for $Re=200$.

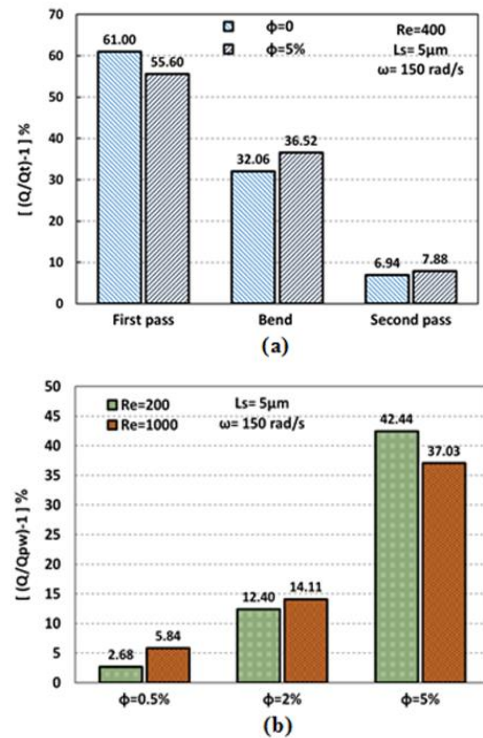


Fig. 9. (a) The share of average heat transfer rate in the first pass, second pass and bend region of the microchannel ($Re=400, \omega=300 \text{ rad/s}, L_s=5 \mu m$) for the pure water and water/ Al_2O_3 ($\phi = 5\%$), (b) the average heat transfer of nanofluid at $Re=200$ and $Re=1000$ for different volume concentrations, ϕ (normalized with the average heat transfer for pure water at the corresponding Re).

Figure 10(a) shows the normalized pressure drop variations with Reynolds number in the microchannel for various volume concentrations, ϕ . In this figure, the normalized pressure drop is scaled with that of pure water flow at corresponding Reynolds number. As is observed, the pressure drop ratio increases with increasing ϕ , while its variation with Re is small. For example, at $Re=600$, the normalized pressure drop for the nanofluid flow at concentrations of $\phi = 0.5, 2$ and 5% are 1.1, 1.4, and 2.5 times of those obtained for pure water, respectively. Figure 10(b) shows the normalized pressure drop (normalized with that of the pure water at $Re=200$) variation with Reynolds number for

different ϕ . This figure illustrates that the normalized pressure drop of microchannel increases with Reynolds number and volume concentration, ϕ . For example at $Re=1000$, the normalized pressure drops of nanofluid with volume concentration from $\phi = 0.5$ to 5 % increase about 7-10 times of that of pure water at $Re=200$.

In fact, the increase of pressure drop for nanofluid flow in comparison with that of pure water flow for the same values of slip length for both fluids is due to the increase in viscosity and slip velocity at the microchannel walls. To show this point in more details, we consider approximately the shear stress forces on the microchannel walls identical to the total pressure force of the microchannel ($\Delta P \times A_c = \tau_w \times A$), where the shear stress is defined as $\tau_w = \mu \times (\partial u / \partial n)$. Based on Eq. (4), the velocity gradient is proportional to the slip velocity for the same value of slip length for both fluids. Thus, the nanofluid to water pressure drop ratio can be simplified as Eq. (21), where A_c and A are similar for two fluids flow.

$$\frac{\Delta P_{nf}}{\Delta P_{water}} = \frac{\tau_{w,nf}}{\tau_{w,water}} = \frac{\mu_{nf}}{\mu_{water}} \times \frac{u_{s,nf}}{u_{s,water}} \quad (21)$$

Equation (21) shows that the pressure drop in the nanofluid (as compared with the corresponding value for pure water flow) increases partly due to the increase of viscosity and also the slip velocity for the same slip length at the walls (see also Fig. 4). For example, for $\phi = 5\%$, $L_s=5\ \mu m$ and $Re=200$ in Fig. 10(a), the pressure drop of the nanofluid flow is 2.4 times of that of the water flow, and the viscosity ratio of the nanofluid ($\phi = 5\%$) to pure water is about $\mu_{nf}/\mu_{water} = 1.7$. Therefore, according to Eq. (21), the ratio of average slip velocities for both fluids at the microchannel walls is $u_{s,nf}/u_{s,water} = 1.4$. This example shows that the viscosity and slip velocity increase have considerable effect on the nanofluid flow pressure drop (as compared with pure water). However, the increase of the viscosity would be more effective than the slip velocity augmentation in this regard.

The heat transfer rate and pressure drop are two important parameters of a thermal system such as microchannel. To judge about the suitability of the results, a balance between the pressure drop or power consumed and heat transfer augmentation is examined as a criterion which is denoted as the thermal performance coefficient (see Eqs. (10) and (12)). In this study, the reference case (denoted as subscript of *ref* in Eqs. (10) and (12)) is considered that of water flow at the corresponding Reynolds number. In fact, this criterion represents the performance of a microchannel with the water/ Al_2O_3 nanofluid flow in comparison with that of pure water. A thermal performance coefficient higher than one is preferable case which shows increase in the heat transfer is high enough to compensate the increase at pressure drop or power consumed. If the pressure drop is not the main concern and the enhancement of heat transfer rate is considered as the main factor for choosing a thermal system, thus a lower thermal performance coefficient is also acceptable.

Figures 11(a) and (b) show the thermal performance coefficient for various volume concentration, ϕ , and Reynolds numbers. C -coefficient in the Eq. (11) represents properties ratio of the fluids (water and nanofluid). In fact, if main and reference fluids are identical (e.g. water) in calculating the thermal performance coefficient, thus C -coefficient becomes equal to one. The results in Fig. 11(a) were obtained from Eq. (10), where the C -coefficient is considered, while in Fig. 11(b) C -coefficient is set to one. Fig. 11(a) shows that the thermal performance coefficient decreases by increasing ϕ for all Reynolds numbers employed. This reduction is due to a higher increase in the pressure drop for higher ϕ , see Fig. 10. For example, the thermal performance coefficient at concentrations of $\phi = 0.5, 2,$ and 5% at $Re=200$ are 1.11, 1.03, and 0.81, respectively. These results emphasize that using the water/ Al_2O_3 nanofluid at lower volume concentrations provides the thermal performance coefficient greater than one. As seen from Fig. 11(a), a slight reduction occurs in the performance coefficient by increasing the Reynolds number from 200 to 1000. The C -coefficient is varied from about 1.1 to 0.86 by increasing ϕ from 0.5% to 5% (Fig. 11(a)). Thus, an overestimation or underestimation value for thermal performance coefficient is predicted by ignoring the property ratio of two fluids as used by most of previous publications, compare Figs. 11(a) and 11(b).

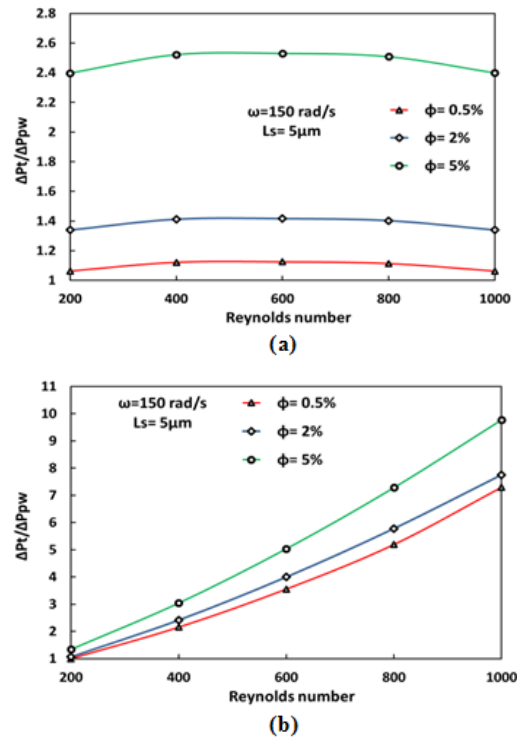


Fig. 10. Variation of the normalized pressure drop in microchannel with Reynolds number and volume concentration ($\omega=150\ rad/s, L_s=5\ \mu m$), (a) normalized by that of pure water flow at the corresponding Reynolds number, (b) normalized by that of pure water at $Re=200$.

Based on Fig. 11(a), we concluded that if the

pressure drop is significant as heat transfer enhancement in a thermal system, using nanofluids at low volume concentrations are favorable. In many thermal systems, obtaining a higher heat transfer rate is main concern, thus employing nanofluid as working fluid is desirable.

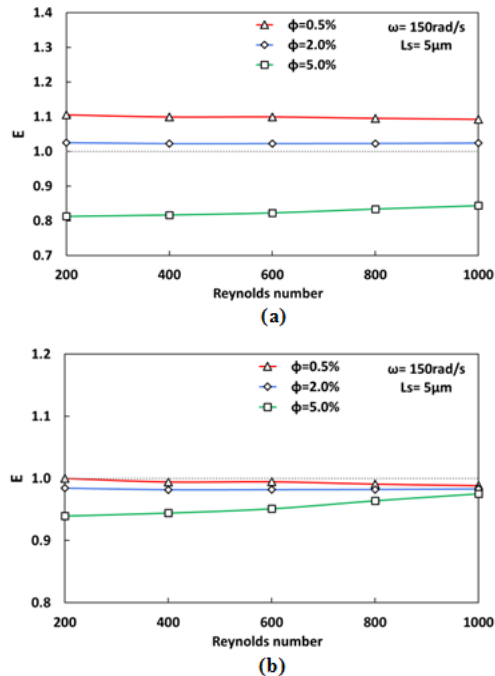


Fig. 11. Thermal performance coefficients for different Reynolds numbers and volume concentrations, ϕ , (a) calculated by Eq. (10), where $C \neq 1$, (b) calculated by Eq. (12), where $C = 1$.

6. CONCLUSION

This work provides numerical results of flow and heat transfer in a three-dimensional rotating U-shaped microchannel with square cross-section. Water and water/ Al_2O_3 nanofluid are considered as working fluids. The effects of many parameters including slip flow, rotational speed, and Reynolds number are investigated. Some findings are presented as follows:

- For a specific slip length and Reynolds number, the slip velocity in nanofluid flow is larger than that of pure water flow due to the increase of velocity gradient on the walls.
- The first pass and the bend region of microchannel have the largest share of average heat transfer while the second pass has a lower value. If the nanofluid (especially in high volume concentrations) is used as working fluid, the share of the bend region and the outlet pass in heat transfer slightly increases. The share of outlet pass in the average heat transfer increases from 3 to 10% from Reynolds number of 200 to 1000.
- If the main and reference fluids are not similar, using Eqs. (13) or (12) can provide rough

estimation of the thermal performance coefficient. For such cases, Eq. (10) should be employed.

- To judge about the suitability of the results, a balance between the pressure drop or power consumed and heat transfer augmentation is examined as a criterion, which is denoted as the thermal performance coefficient. Most of the previous publications were employed a version of this criterion where the physical properties of both fluids were considered similar. If the main and reference fluids are not similar (e.g. water and water/ Al_2O_3 nanofluid), a rough estimation of the thermal performance coefficient is achieved. The modified version of this criterion is employed in this work, where this correction can change the thermal performance coefficient from about +10% at $\phi = 0.5\%$ to -14% at $\phi = 5\%$.
- For $\phi = 0.5$ and 2% water/ Al_2O_3 nanofluids as the working fluid, the thermal performance coefficients increase about 10 and 5%, respectively. However, the thermal performance coefficient for $\phi = 5\%$ water/ Al_2O_3 nanofluid reduces about 14% as compared with the pure water working fluid. This trend is almost identical for all Reynolds numbers employed.
- In problems where pressure drop is especially important, using nanofluids at low volume concentrations are favorable. Nevertheless, a significant increase (about 40%) in heat transfer is achieved by nanofluid with $\phi = 5\%$ (as compared with water). Such augmentation in heat transfer is a main reason for using nanofluids in thermal systems. In fact, if the heat transfer rate is considered as the main criterion for selecting a thermal system, using nanofluid flow with high volume concentrations is suggested as an appropriate heat transfer enhancement method.

REFERENCES

- Ahmed, M. and M. Eslamian (2015). Laminar Forced Convection of a Nanofluid in a Microchannel: Effect of Flow Inertia and External Forces on Heat Transfer and Fluid Flow Characteristics. *Applied Thermal Engineering* 78, 326-338.
- Al-Qahtani, M., Y.J. Jang, H.C. Chen and J.C. Han (2002). Flow and heat transfer in rotating two-pass rectangular channels ($AR=2$) by Reynolds stress turbulence model. *International Journal of Heat and Mass Transfer* 45, 1823-1838.
- Arkles, B. (2011). Hydrophobicity, Hydrophilicity and Silane Surface Modification. *Gelest Inc* 215, 547-1015.
- Barrat, J. L. and F. Chiaruttini (2003). Kapitza resistance at the liquid solid interface. *Molecular Physics* 101, 1605-1610.

- Behfar, M. and A. Sohankar (2016). Numerical investigation for finding the appropriate design parameters of a fin-and-tube heat exchanger with delta-winglet vortex generators. *Heat Mass Transfer* 52, 21–37.
- Bergles, A. E. (1997). Heat Transfer Enhancement—The Maturing of Second-Generation Heat Transfer Technology. *International Journal of Heat and Mass Transfer* 18, 47–55.
- Bergles, A. E. (2000). Some Perspectives on Enhanced Heat Transfer, Second-Generation Heat Transfer Technology. *International Journal of Heat and Mass Transfer* 110, 1082–1096.
- Choi, C.H., K. Johan, A. Westin and S. Breuer (2002). To slip or not slip-Water flows in hydrophilic and hydrophobic microchannels. *ASME (International Mechanical Engineering Congress & Exposition)* 557-564.
- Corcione, M., M. Cianfrini and A. Quintino (2013). Optimization of laminar pipe flow using nanoparticle liquid suspensions for cooling applications. *Applied Thermal Engineering* 50, 857-867.
- Cowley, A., D. Maynes and J. Crockett (2014). Effective temperature jump length and influence of axial conduction for thermal transport in superhydrophobic channels. *International Journal of Heat and Mass Transfer* 79, 573–583.
- Duan, Z. and Y. S. Muzychka (2007). Slip flow in non-circular microchannels. *Microfluid Nanofluid* 3, 473-48.
- Eslamian, M. and M. Ziad Saghir (2014). On thermophoresis modeling in inert nanofluids. *International Journal of Thermal Sciences* 80, 58-64.
- Eslamian, M., M. Ahmed, M.F. El-Dosoky and M.Z. Saghir (2015). Effect of thermophoresis on natural convection in a Rayleigh–Benard cell filled with a nanofluid. *International Journal of Heat and Mass Transfer* 81,142-156.
- Hung, T.C., W.M. Yan, X.D. Wang and C.Y. Chang (2012). Heat transfer enhancement in microchannel heat sinks using nanofluid. *International Journal of Heat and Mass Transfer* 55, 2559-2570.
- Kalteh, M., A. Abbassi, M. Saffar-Avval, A. Frijns, A. Darhuber and J. Harting (2012). Experimental and numerical investigation of nanofluid forced convection inside a wide microchannel heat sink. *Applied Thermal Engineering* 36, 260-268.
- Kanikzadeh, M. and A. Sohankar (2016a). Numerical Investigation of Forced Convection Flow of Nanofluids in Rotating U-Shaped Smooth and Ribbed Channels. *Heat Transfer Engineering Journal* 37, 840-86.
- Kanikzadeh, M. and A. Sohankar, (2016b). Thermal performance evaluation of the rotating U-shaped micro/mini/macro channels using water and nanofluids. *Numer. Heat Transfer* 70, 650–672.
- Karniadakis, G., Beskok, A., Aluru, N. R. (2005). "Microflows and Nanoflows-Fundamentals and Simulation", Springer Verlag 29.
- Kundu, M., K. Vamsee and D. Maiti (2009). Simulation and analysis of flow through micro channel. *Asia-Pacific Journal of Chemical Engineering* 4(4), 450-461.
- Lee, J. and I. Mudawar (2007). Assessment of the effectiveness of nanofluids for single-phase and two-phase heat transfer in micro-channels. *International Journal of Heat and Mass Transfer* 50, 452–463.
- Manca, O., S. Nardini and D. Ricci (2012). A numerical study of nanofluid forced convection in ribbed channels. *Applied Thermal Engineering* 37, 280-292.
- Maynes, D. and Crockett, J. (2014). Apparent Temperature Jump and Thermal Transport in Channels With Streamwise Rib and Cavity Featured Superhydrophobic Walls at Constant Heat Flux. *Journal of Heat Transfer (ASME)* 136, 011701.
- Maynes, D., B.W. Webb, J. Crockett and V. Solovjov (2013). Analysis of laminar slip-flow thermal transport in microchannels with transverse rib and cavity structured superhydrophobic walls at constant heat flux. *Journal Heat Transfer (ASME)* 135 (2), 021701.
- Mirzaei, M., Sohankar, A. (2013a) "Heat transfer augmentation in plate finned tube heat exchangers with vortex generators: A comparison of round and flat tubes", Iranian Journal of Science and Technology, Transactions of Mechanical Engineering 37, 39-51.
- Mirzaei, M., Davidson, L., Sohankar, A., Innings, F. (2013b). "The effect of corrugation on heat transfer and pressure drop in channel flow with different Prandtl numbers", International Journal of Heat and Mass Transfer., 66, 164–176.
- Mirzaei, M., Sohankar, Davidson, L., A., Innings, F. (2014). "Large Eddy simulation of the flow and heat transfer in a half-corrugated channel with various wave amplitudes", Int. J. Heat Mass Transf., vol. 76, pp. 432–446.
- Raisi, A., B. Ghasemi and S. M. Aminossadati (2011). A Numerical Study on the Forced Convection of Laminar Nanofluid in a Microchannel with Both Slip and No-Slip Conditions. *Numerical Heat Transfer, Part A: Applications* 59(2), 114-129.
- Roy, P., N. K. Anand and D. Banerjee (2013a). Liquid slip and heat transfer in rotating rectangular microchannels. *International Journal of Heat and Mass Transfer* 62, 184-199.

- Roy, P., N. K. Anand and D. Banerjee (2013b). A Review of flow and heat transfer in rotating microchannels. *Procedia Engineering* 56, 7–17.
- Saha, S. K., G. P. Celeta and S. Wongwises (2012). Selected Papers on Advances in Heat Transfer. *Heat Transfer Engineering* 33, 281- 283.
- Shah, R. K. and D. P. Sekulic (2003). Fundamentals of heat exchanger design. John Wiley and Sons, Hoboken, New Jersey.
- Sohankar, A. (2007). Heat transfer augmentation in a rectangular channel with a vee-shaped vortex generator. *International Journal of Heat and Fluid Flow* 28, 306–317.
- Sohankar, A., M. Riahi and E. Shirani (2017). Numerical investigation of heat transfer and pressure drop in a rotating U-shaped hydrophobic microchannel with slip flow and temperature jump boundary conditions. *Applied Thermal Engineering* 117, 308–321.
- Suresh, S., M. Chandrasekar and S. Chandra Sekhar (2011). Experimental studies on heat transfer and friction factor characteristics of CuO/water nanofluid under turbulent flow in a helically dimpled tube. *Experimental Thermal and Fluid Science* 35, 542–549.
- Tretheway, D.C. and C.D. Meinhart (2002). Apparent fluid slip at hydrophobic microchannel walls. *Physics of fluids* 14(2), 9-12.
- Vajjha, R. S. and D.K. Das (2009). Experimental determination of thermal conductivity of three nanofluids and development of new correlations. *International Journal of Heat and Mass Transfer* 52, 4675–4682.
- Watanabe, K. and H. Mizunuma (1998). Slip of Newtonian fluids at solid boundary. *SME International Journal Series B Fluids and Thermal Engineering* 41, 525–529.
- Webb, R. L., Kim, N. H. (2005). “Principles of Enhanced Heat Transfer”, 2nd ed., Taylor & Francis Group, New York, NY.
- Xiao, N., J. Elsnab and T. Ameel (2009). Microtube gas flows with second-order slip flow and temperature jump boundary conditions. *International Journal of Thermal Sciences* 48, 243-251.
- Yari Ghale, Z.M. Haghshenasfard and M. Nasr Esfahany (2015). Investigation of nanofluids heat transfer in a ribbed microchannel heat sink using 2 single-phase and multiphase CFD models. *International Communications in Heat and Mass Transfer* 68, 122–129.